NASA/TM—2015-218740

Investigation of Micro-Scale Architectural Effects on Damage of Composites

Bertram Stier
RWTH Aachen University, D-52074 Aachen, Germany

Brett A. Bednarcyk
Glenn Research Center, Cleveland, Ohio

Jaan W. Simon and Stefanie Reese
RWTH Aachen University, D-52074 Aachen, Germany

May 2015

NASA STI Program . . . in Profile

Since its founding, NASA has been dedicated to the advancement of aeronautics and space science. The NASA Scientific and Technical Information (STI) Program plays a key part in helping NASA maintain this important role.

The NASA STI Program operates under the auspices of the Agency Chief Information Officer. It collects, organizes, provides for archiving, and disseminates NASA's STI. The NASA STI Program provides access to the NASA Technical Report Server—Registered (NTRS Reg) and NASA Technical Report Server—Public (NTRS) thus providing one of the largest collections of aeronautical and space science STI in the world. Results are published in both non-NASA channels and by NASA in the NASA STI Report Series, which includes the following report types:

- TECHNICAL PUBLICATION. Reports of completed research or a major significant phase of research that present the results of NASA programs and include extensive data or theoretical analysis. Includes compilations of significant scientific and technical data and information deemed to be of continuing reference value. NASA counter-part of peer-reviewed formal professional papers, but has less stringent limitations on manuscript length and extent of graphic presentations.

- TECHNICAL MEMORANDUM. Scientific and technical findings that are preliminary or of specialized interest, e.g., "quick-release" reports, working papers, and bibliographies that contain minimal annotation. Does not contain extensive analysis.

- CONTRACTOR REPORT. Scientific and technical findings by NASA-sponsored contractors and grantees.

- CONFERENCE PUBLICATION. Collected papers from scientific and technical conferences, symposia, seminars, or other meetings sponsored or co-sponsored by NASA.

- SPECIAL PUBLICATION. Scientific, technical, or historical information from NASA programs, projects, and missions, often concerned with subjects having substantial public interest.

- TECHNICAL TRANSLATION. English-language translations of foreign scientific and technical material pertinent to NASA's mission.

For more information about the NASA STI program, see the following:

- Access the NASA STI program home page at http://www.sti.nasa.gov

- E-mail your question to help@sti.nasa.gov

- Fax your question to the NASA STI Information Desk at 757-864-6500

- Telephone the NASA STI Information Desk at 757-864-9658

- Write to:
  NASA STI Program
  Mail Stop 148
  NASA Langley Research Center
  Hampton, VA 23681-2199

NASA/TM—2015-218740

Investigation of Micro-Scale Architectural Effects on Damage of Composites

Bertram Stier
RWTH Aachen University, D-52074 Aachen, Germany

Brett A. Bednarcyk
Glenn Research Center, Cleveland, Ohio

Jaan W. Simon and Stefanie Reese
RWTH Aachen University, D-52074 Aachen, Germany

National Aeronautics and
Space Administration

Glenn Research Center
Cleveland, Ohio 44135

May 2015

Level of Review: This material has been technically reviewed by technical management.

Available from

NASA STI Program
Mail Stop 148
NASA Langley Research Center
Hampton, VA 23681-2199

National Technical Information Service
5285 Port Royal Road
Springfield, VA 22161
703-605-6000

This report is available in electronic form at http://www.sti.nasa.gov/ and http://ntrs.nasa.gov/

Investigation of Micro-Scale Architectural Effects on Damage of Composites

Bertram Stier
Institute of Applied Mechanics
RWTH Aachen University
Mies-van-der-Rohe-Straβe 1
D-52074 Aachen, Germany

Brett A. Bednarcyk
National Aeronautics and Space Administration
Glenn Research Center
Cleveland, Ohio 44135

Jaan W. Simon and Stefanie Reese
Institute of Applied Mechanics
RWTH Aachen University
Mies-van-der-Rohe-Straβe 1
D-52074 Aachen, Germany

Abstract

This paper presents a three-dimensional, energy based, anisotropic, stiffness reduction, progressive damage model for composite materials and composite material constituents. The model has been implemented as a user-defined constitutive model within the Abaqus finite element software package and applied to simulate the nonlinear behavior of a damaging epoxy matrix within a unidirectional composite material. Three different composite microstructures were considered as finite element repeating unit cells, with appropriate periodicity conditions applied at the boundaries. Results representing predicted transverse tensile, longitudinal shear, and transverse shear stress-strain curves are presented, along with plots of the local fields indicating the damage progression within the microstructure. It is demonstrated that the damage model functions appropriately at the matrix scale, enabling localization of the damage to simulate failure of the composite material. The influence of the repeating unit cell geometry and the effect of the directionality of the applied loading are investigated and discussed.

1. Introduction

Progressive damage modeling of polymer matrix composites has received a great deal of attention in recent years as predictive capabilities for the complex nonlinear behavior of these materials are sought. A significant outstanding question is in regards to the proper, or most beneficial, scale on which the material damage model should function. Modeling the composite at the scale of the constituents (i.e., fiber and matrix materials) enables use of models for the matrix material that are initially isotropic and avoids ad-hoc coupling rules for the various damage components. However, a validated micromechanics method is required, and often, the constituent scale data best suited for characterizing the damage model are unavailable. In contrast, the macro-scale approach, wherein the composite is treated as an effective anisotropic material, will always be more computationally efficient, yet it requires a more complex damage model to handle the extreme anisotropy of the composite material with its directionally dependent multiple damage mechanisms. Further, the way in which the damage components interact (i.e., how much shear stiffness reduction results from a given amount of normal stiffness reduction) must be characterized, or, more commonly, assumed.

Herein, an anisotropic, three-dimensional, progressive damage model, capable of modeling composites at the macro (composite) scale, as well as at the micro (constituent) scale, is presented. The development follows the approach outlined by Barbero [1] in the case of plane stress. The damage model uses the continuum damage approach first introduced by Kachanov [2, 3] in which continuous damage variables are introduced to quantify the stiffness reduction of a material in various directions. The theoretical background of this approach, and specifically, the elastic stiffness reduction damage approach, is discussed in detail by Lemaitre [5] and Chaboche [6], Kruch and Chaboche [18], Kajcinovic [7], Voyiadjis and Kattan [8], and Talreja [9, 10]. Further, Ladevéze [14, 15] and Pineda et al. [12] have reported progressive stiffness reduction damage models aimed at polymer matrix composites at the composite level. These models are motivated by the microstructure, but cannot consider micro scale effects like random fiber distribution and void content/morphology. Pineda et al. [11] and Bednarcyk et al. [13] presented stiffness reduction

damage models operating at the micro (fiber/marix) scale, but these studies did not examine micro scale architectural effects. Micromechanical investigations considering random fiber distributions of unidirectional (UD) fiber reinforced plastics (FRP) using an elasto-plastic isotropic damage model for the matrix material with the focus on fiber-matrix debonding were carried out by Melro et. al. [16, 17]. Chen and Ghosh [19] studied the strain rate dependent deformation and failure of composite materials at the micro-scale for different ideally packed unit cells under different strain rates and loading conditions. However, none of these works studied the influence of the coupling of the damage variables.

The progressive damage model presented below is characterized for a polymer resin based on neat matrix tensile data. The model has been implemented within Abaqus [4] and applied to model the matrix material within a unidirectional polymer matrix composite. Three different composite repeating unit cells (with constant fiber volume fraction), representing three different fiber architectures, have been considered: hexagonal dense packing (i.e., equilateral hexagonal packing), and 5 and 15 fiber repeating unit cells (RUCs) with random fiber packing. The boundary conditions necessary to enforce periodicity at the RUC boundaries, while preserving the ability to apply arbitrary global (far-field) strains, are also presented. Results are shown for the three RUC microstructures for applied transverse tension, longitudinal shear, and transverse shear as a function of a damage model parameter that controls the extent of shear damage. The functionality of the damage model and its ability to predict damage localization, are highlighted, as are the effects of the directionality of the applied transverse tension and longitudinal shear loading, with respect to the RUC geometries.

2. Progressive Damage Model

A stiffness reduction progressive damage model has been developed and implemented based on the two-dimensional approach given by Barbero [1]. For application to the matrix material within a composite, a three-dimensional extension of the model is needed due to the local three-dimensional stress state within a composite material. For a pure monolithic matrix, it is reasonable to consider the material to be initially isotropic, however when subjected to deformation, the formulation enables the material to exhibit anisotropic behavior depending on the activation (influence) of the damage mechanisms in the different directions. To allow for arbitrary damage, the in situ material model should have the capability to allow for different coupling of the damage variables, to represent, for example, penny shaped cracks or cavity type damage. The consequence is a very general formulation of the damage model, wherein the physical interpretation of the material parameters is maintained. The model is based on the principle of energy equivalence [2] for small strains, and utilizes six scalar damage variables associated with the Young's and shear moduli. Thus, the proposed Gibbs free energy is given by,

$$\begin{aligned}\chi =& \frac{1}{2\rho}[\frac{\sigma_{11}^2}{(1-D_1)^2\tilde{E}_1}+\frac{\sigma_{22}^2}{(1-D_2)^2\tilde{E}_2}+\frac{\sigma_{33}^2}{(1-D_3)^2\tilde{E}_3}\\ &-(\frac{\tilde{\nu}_{21}}{\tilde{E}_2}+\frac{\tilde{\nu}_{12}}{\tilde{E}_1})\frac{\sigma_{11}\sigma_{22}}{(1-D_1)(1-D_2)}\\ &-(\frac{\tilde{\nu}_{31}}{\tilde{E}_3}+\frac{\tilde{\nu}_{13}}{\tilde{E}_1})\frac{\sigma_{11}\sigma_{33}}{(1-D_1)(1-D_3)}\\ &-(\frac{\tilde{\nu}_{32}}{\tilde{E}_3}+\frac{\tilde{\nu}_{23}}{\tilde{E}_2})\frac{\sigma_{22}\sigma_{33}}{(1-D_2)(1-D_3)}\\ &+\frac{\sigma_{12}^2}{(1-D_{12})2\tilde{G_{12}}}+\frac{\sigma_{13}^2}{(1-D_{13})2\tilde{G_{13}}}+\frac{\sigma_{23}^2}{(1-D_{23})2\tilde{G_{23}}}]\end{aligned} \tag{1}$$

where ρ is the density of the material, σ_{ij} are the stress components, $\boldsymbol{D} = [D_{11}D_{22}D_{33}D_{12}D_{13}D_{23}]$ are the damage variables, and $\tilde{E}_i$, $\tilde{G}_{ij}$ and $\tilde{\nu}_{ij}$ are the pristine (undamaged) Young's moduli, shear moduli, and Poisson's ratios, respectively. The material compliance tensor, $\boldsymbol{S}$, is then given by the second derivative of the Gibbs free energy with respect to the stress tensor,

$$\boldsymbol{S} = \rho\frac{\partial^2\chi}{\partial\boldsymbol{\sigma}^2} \tag{2}$$

The formulation relies on a damage surface, $g(\boldsymbol{Y}(\boldsymbol{D}), \gamma(\delta))$, and a damage potential, $f(\boldsymbol{Y}(\boldsymbol{D}), \gamma(\delta))$, which are functions of thermodynamic forces, $\boldsymbol{Y}$, and a hardening/softening function, $\gamma(\delta)$, with δ being the damage hardening/softening variable. Moreover, it is associative, which requires $f = g$. When damage is accumulating,

$$f = g = \hat{g} - \hat{\gamma} = 0 \tag{3}$$

with

$$\hat{g} = \sqrt{\boldsymbol{Y}\boldsymbol{H}\boldsymbol{Y}} \tag{4}$$

$$\hat{\gamma} = \gamma + \gamma_0 = c_1(e^{\frac{\delta}{c_2}} - 1) + \gamma_0 \tag{5}$$

where c_1 and c_2 are material constants, γ_0 is the damage threshold, and $\boldsymbol{H}$ is a matrix of material parameters responsible for the interaction of the damage variables' effect on the stiffness reduction of the material. If f is less than zero, damage does not evolve.

The vector of thermodynamic driving forces is given by

$$\boldsymbol{Y} = \rho \frac{\partial \chi}{\partial \boldsymbol{D}} \tag{6}$$

and the damage evolution is

$$\dot{\boldsymbol{D}} = \dot{\lambda} \frac{\partial f}{\partial \boldsymbol{Y}} \tag{7}$$

where the Lagrangian (damage) multiplier $\dot{\lambda}$ can be interpreted as the damage rate magnitude and $\frac{\partial f}{\partial \boldsymbol{Y}}$ is the direction of damage evolution in $\boldsymbol{Y}$-space. Further, the damage rate magnitude affects the hardening variable rate as

$$\dot{\delta} = \dot{\lambda} \frac{\partial g}{\partial \gamma} \tag{8}$$

Making use of the consistency condition

$$\dot{g} = \frac{\partial g}{\partial \boldsymbol{Y}} \dot{\boldsymbol{Y}} + \frac{\partial g}{\partial \gamma} \dot{\gamma} = 0 \tag{9}$$

the Lagrange (damage) multiplier can be obtained

$$\dot{\lambda} = - \frac{\frac{\partial g}{\partial \boldsymbol{Y}} \frac{\partial \boldsymbol{Y}}{\partial \boldsymbol{\varepsilon}}}{\frac{\partial g}{\partial \boldsymbol{Y}} \frac{\partial \boldsymbol{Y}}{\partial \boldsymbol{D}} \frac{\partial f}{\partial \boldsymbol{Y}} + \frac{\partial \gamma}{\partial \delta}} \dot{\boldsymbol{\varepsilon}} \tag{10}$$

where $\boldsymbol{\varepsilon}$ is the strain tensor. Then, the damage variable evolution can be calculated from (7). Finally, from (3), (5) and (8), the hardening variable evolution is

$$\dot{\delta} = -\dot{\lambda} \tag{11}$$

A standard return mapping algorithm with an elastic predictor/damage corrector strategy was used for the numerical implementation into the UMAT user material routine of the commercial FE software Abaqus [4].

3. Damage Interaction

Based on (7) and (3-5), the evolution of one damage component is

$$\dot{D}_1 = \dot{\lambda} \frac{\partial \hat{g}}{\partial \boldsymbol{Y}} = \frac{\dot{\lambda}}{2\hat{g}} [2H_{11}Y_1 + (H_{12}H_{21})Y_2 + (H_{13}H_{31})Y_3 + (H_{14}H_{41})Y_4 + (H_{15}H_{51})Y_5 + (H_{16}H_{61})Y_6] \tag{12}$$

Thus, a uniaxial stress, which will produce only one component of $\boldsymbol{Y}$ (see (6) and (1)), denoted by Y_j, will induce damage in 1-direction, provided H_{1j} is non-zero. Thus, to simulate a fracture mechanics type interaction (penny

shaped crack), H_{11}, H_{14}, and H_{15} can be chosen as non-zero. Then, σ_{11}, σ_{12}, and σ_{13}, would induce damage that would cause a stiffness reduction in the 11-, 12- and 13-components. Conversely, if the damage evolution of the material is assumed to be isotropic, then the components H_{ij} can be chosen as,

$$\begin{aligned} &H_{11} = H_{22} = H_{33} = H_{nn} \\ &H_{14} = H_{41} = H_{24} = H_{42} = H_{15} = H_{51} = H_{35} = H_{53} = H_{26} = H_{62} = H_{36} = H_{63} = H_{sn} \\ &H_{44} = H_{55} = H_{66} = H_{ss} \end{aligned} \tag{13}$$

In addition to specification of these **H** matrix terms, c_1, c_2 and γ_0 must be chosen to fully characterize the damage model.

4. Damage Model Characterization

The damage model was characterized for tension through correlation with a cyclic tension test on a neat epoxy resin material (RIMR 135/RIMH 137, mass mixing ratio 10:3, 8 hr curing time at 40° C). The epoxy was vacuum injected into a standard dogbone mold to minimize voids. Cyclic tension was achieved using a constant crosshead speed of $10mm/s$, with strains measured via a digital image correlation system.

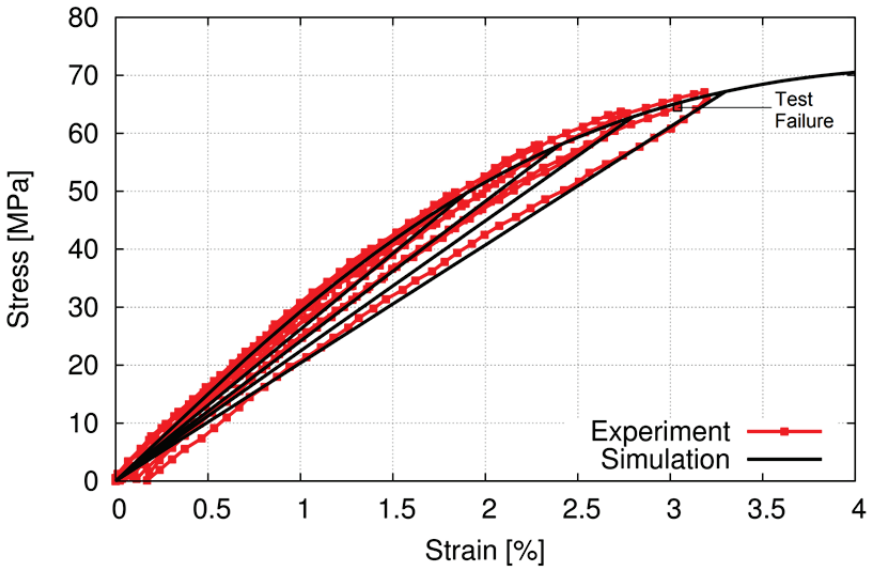

Figure 1: Model correlation with epoxy tensile test data

The model characterization is shown in Figure 1. Note that the test specimen failed suddenly during the final reloading cycle at the point indicated. Furthermore, the nonlinear resin response appears to be due to both inelastic deformation and damage mechanisms as some permanent deformation is observed after unloading, albeit small. In the present formulation all nonlinear behavior is assumed to be associated with damage only. Since the damage model is based purely on stiffness reduction, upon unloading, there is zero permanent strain. This is a reasonable approximation of the actual epoxy tensile response as only a small amount of permanent strain was evident upon unloading. Based on the correlation shown, the isotropic elastic properties and damage model parameters obtained for the epoxy are shown in Table 1.

The Poisson's ratio of the epoxy given in Table 1 was not measured, but set to a typical value. The influence of the shear damage parameter, H_{ss}, will be examined via parametric studies on a unidirectional composite repeating unit cell.

Table 1: Material parameters for RIMR 135/RIMH 137 epoxy matrix

Matrix	
E	$3000\,MPa$
ν	0.38
c_1	$27.5\,MPa$
c_2	-2.8
H_{nn}	0.75
γ_0	$0.45\,MPa$

5. Finite Element Models

The three-dimensional damage model presented above has been implemented into Abaqus [4] as a UMAT user-defined material constitutive routine. To represent a unidirectional composite material, three RUC geometries have been discretized using Abaqus, as shown in Figure 2.

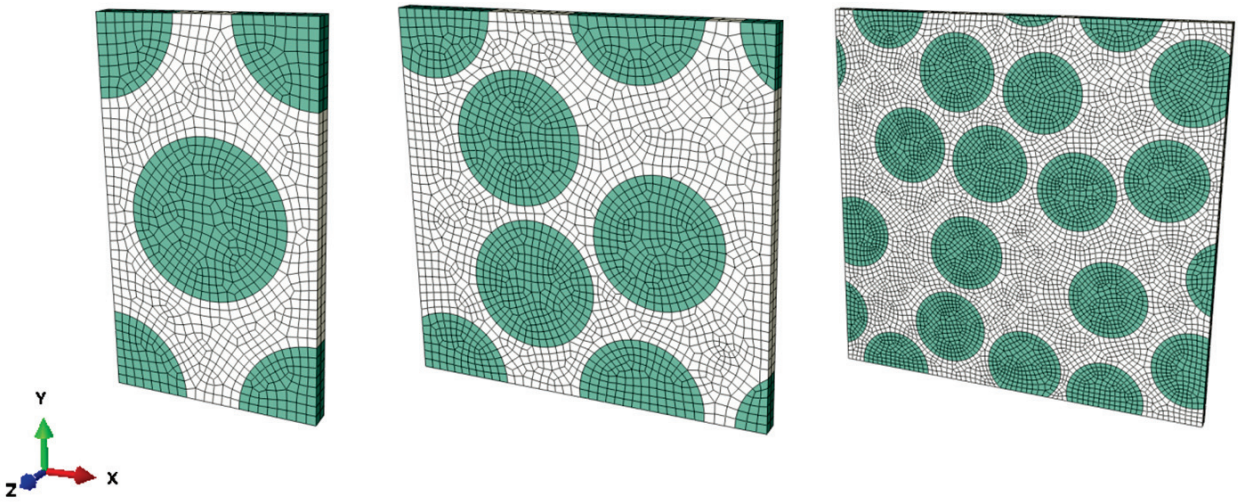

Figure 2: Abaqus finite element model RUCs used to represent a 0.49 fiber volume fraction unidirectional composite. Left: HDP, center: 5 fiber random, right: 15 fiber random

Figure 2 left shows a microstructure with hexagonal dense packing (HDP) meshed with 2,166 C3D8 elements, Figure 2 center contains 5 fibers with random locations meshed with 4,420 C3D8 elements, and Figure 2 right contains 15 fibers with random locations meshed with 13,202 C3D8 elements. In all cases, the fiber volume fraction is 0.49. The fiber is assumed to be carbon; the transversely isotropic elastic properties are shown in Table 2

Table 2: Material parameters for carbon fiber; 1-direction is longitudinal fiber direction

Fiber	
E_1	$290\,GPa$
E_2	$20\,GPa$
ν_{12}	0.2
G_{12}	$20\,GPa$
G_{23}	$9\,GPa$

The influence of external boundaries is removed by imposing periodic boundary conditions. Within Abaqus, this is accomplished using constraint equations, as follows for a parallelepiped model. First, node sets for every node on each face, edge, and vertex must be generated. The nodes at the vertices must not be included in the node sets

associated with edges or faces. Similarly, the nodes at the edges are excluded from the face node sets. Next, the node pairs (two nodes that are coupled via a constraint equation) for the three sets of faces, and the node groups for the three sets of edges, must be identified. The node pair for a face node is always located on the opposite face. For example, referring to Figure 3, a node on face 4 with the coordinates $(x = x_1, y = 0, z = z_1)$ has its partner node on face 2 with $(x = x_1, y = b, z = z_1)$, where b is the length of the RUC in the y-direction. Similarly, the node groups for edges must be determined. The edges are categorized based on direction; for instance, the x-direction edge set includes edges 9, 10, 11 and 12. Then the node groups within each set of edges are found at the same coordinate along the edge direction. For example, a node on edge 9, with the coordinates $(x = x_1, y = 0, z = 0)$ is grouped with nodes on edges 10 $(x = x_1, y = b, z = 0)$, 11 $(x = x_1, y = b, z = c)$ and 12 $(x = x_1, y = 0, z = c)$, where c is the length of the RUC in the z-direction.

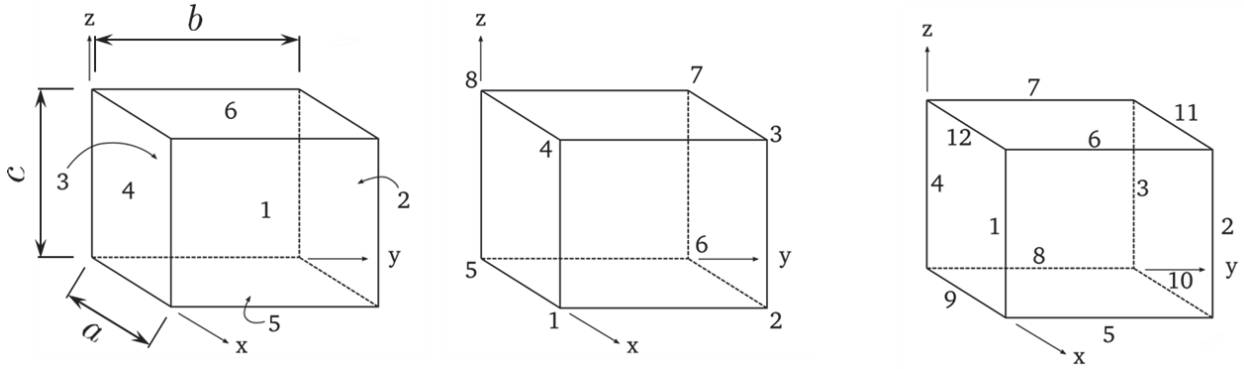

Figure 3: Reference numbering for application of periodic boundary conditions on a parallelepiped finite element model using equation constraints within Abaqus. Left: faces, center: vertices, right: edges

In Abaqus, when coupling nodes via equation constraints, it is only possible to couple the displacements (as opposed to forces). Using three reference points (RPs), designated as RPX at the position of vertex 1, RPY at the position of vertex 6, and RPZ at the position of vertex 8, the complete (arbitrary) far field strain state can be specified by applying displacement boundary conditions to these three RPs.

The equation constraints must be defined such that, for every node pair/group, only one degree of freedom remains in the system, without ever eliminating the same degree of freedom more than once. Denoting the displacement in coordinate direction i and vertex, edge, face, or reference point j as u_i^j, one possibility that accomplishes this is

For edges:

$$
\begin{aligned}
u_i^1 - u_i^4 - u_i^{RPX} &= 0 \\
u_i^2 - u_i^4 - u_i^{RPX} - u_i^{RPY} &= 0 \\
u_i^3 - u_i^4 - u_i^{RPY} &= 0 \\
u_i^5 - u_i^8 - u_i^{RPX} &= 0 \\
u_i^6 - u_i^8 - u_i^{RPX} - u_i^{RPZ} &= 0 \\
u_i^7 - u_i^8 - u_i^{RPZ} &= 0 \\
u_i^{10} - u_i^9 - u_i^{RPX} &= 0 \\
u_i^{11} - u_i^9 - u_i^{RPX} - u_i^{RPY} &= 0 \\
u_i^{12} - u_i^9 - u_i^{RPY} &= 0
\end{aligned}
$$

For faces:

$$
\begin{aligned}
u_i^1 - u_i^3 - u_i^{RPX} &= 0 \\
u_i^2 - u_i^4 - u_i^{RPY} &= 0 \\
u_i^6 - u_i^5 - u_i^{RPZ} &= 0
\end{aligned}
$$

For vertices:

$$
\begin{aligned}
u_i^1 - u_i^{RPX} &= 0 \\
u_i^2 - u_i^{RPX} - u_i^{RPY} &= 0 \\
u_i^3 - u_i^{RPX} - u_i^{RPY} - u_i^{RPZ} &= 0 \\
u_i^4 - u_i^{RPX} - u_i^{RPZ} &= 0 \\
u_i^5 &= 0 \\
u_i^6 - u_i^{RPY} &= 0 \\
u_i^2 - u_i^{RPY} - u_i^{RPZ} &= 0 \\
u_i^8 - u_i^{RPZ} &= 0
\end{aligned}
$$

where these equation constraints are imposed on paired and grouped nodes, as described above. Thus, in order to apply a far-field strain, only the displacements of the reference points (RPs), according to the strain state, must be specified as boundary conditions. Figure 4 shows several examples of deformed RUC plots, where the above periodic boundary condition application strategy has been employed. As can be seen, the approach maintains periodicity, even in the presence of significant damage localization.

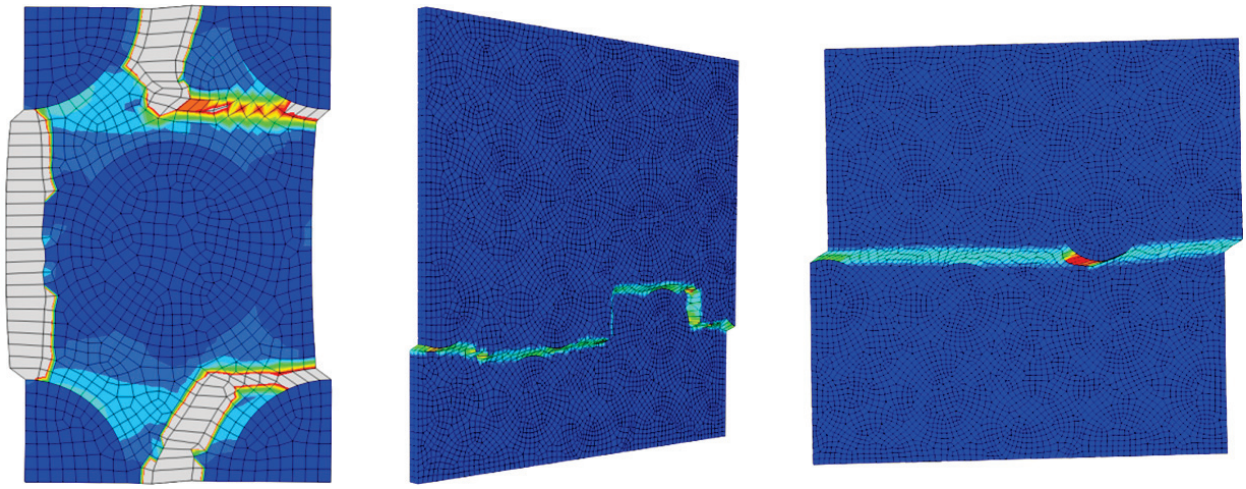

Figure 4: Example deformed plots (deformation scale factor = 5) showing that periodicity is maintained, even in the presence of significant damage localization

It is well-known that, when applying damage models such as this in finite element analysis, pathological mesh-dependence will be present once localization occurs [21, 22]. Thus, for each RUC geometry, it was desired to keep the element size constant during the study. Further, the global element size variation was kept small by restricting the element volume during the discretization process in Abaqus. The element volume and was set to the same value as used in the material calibration step. In the future, length scaling will be added to the model to ensure consistent energy dissipation in the presence of varying mesh sizes [24].

6. Results and Discussion

The impact of the RUC geometry (see Figure 2) on the predicted local and global response of the composite has been examined while also varying the value of the shear damage parameter H_{ss}. For the cases examined, the shear-normal interaction damage parameters,H_{sn}, has been set to zero, eliminating local shear stiffness reduction due to normal stresses as well as normal stress reduction due to shear stresses. Figure 5 shows the predicted transverse tensile response of the composite as a function of the RUC geometry (see Figure 2) and the direction (x or y) of the applied loading for the case of $H_{ss} = 5$. Maximum principal strain fields, which highlight the location of damage within the RUC, are plotted in Figure 6 for five values of the applied global strain. Note that these global strain values are not exact since adaptive time steps were employed in the finite element simulations.

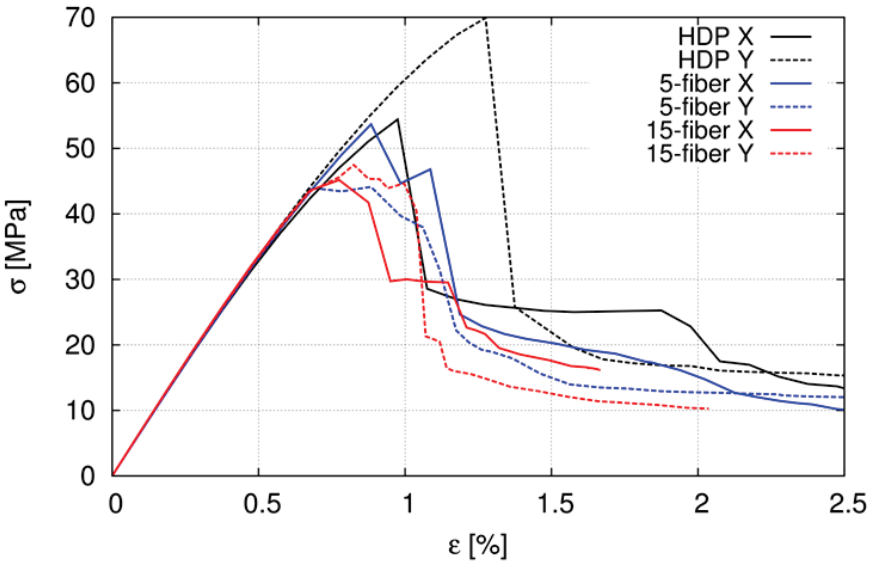

Figure 5: Comparison of the predicted effective composite transverse tensile response as a function of RUC geometry and direction of loading (solid line = loading applied in x-direction, dashed line = loading in the y direction) for the case of $H_{ss} = 5$

While all cases predict nearly identical initial elastic stiffness, once damage initiates, there are significant differences in the global deformation (i.e., damage) response due to microstructural variation in the three RUC representations. For the HDP RUC, there is a large (22%) difference between tensile loading in the x-direction and the y-direction in terms of the stress at which departure from linearity occurs and at which a stress drop occurs. This stress drop is associated with the onset of damage localization within the RUC. As evident in Figure 6, the local fields are different (even initially), which leads to initiation of damage localization much earlier when the HDP RUC is loaded in the x-direction. This is in spite of the fact that, elastically, the RUC behaves transversely isotropically, implying that the average elastic fields are identical for tension in either direction. The final damage patterns are also quite different, with localization progressing completely through the RUC much earlier in the case of y-direction loading as compared to loading in the x-direction.

For the 5 fiber random RUC, Figure 5 shows that, while the difference in the x- and y-direction tensile curve is reduced compared to the HDP RUC, it is still significant (18%). The y-direction loading results in earlier onset of damage localization because of a concentration that arises in the matrix between two fibers that are close together in the y-direction, as can be seen in Figure 6. Both 5 fiber RUC loading simulations exhibit earlier damage localization compared to the HDP RUC simulations due to such concentrations between nearby fibers. In contrast, both 15 fiber RUC loading simulations predict localization at nearly the same time (strain). The damage patterns shown in Figure 6 are qualitatively similar for each level of applied global strain, with the x-direction loading exhibiting a somewhat greater extent of damage localization at the applied global strain of 1%. This is manifested in the somewhat more compliant response after damage initiation in Figure 5. The fact that the x- and y-direction responses are becoming

closer indicates that, as one would expect, as a larger RUC with more fibers is considered, the model provides a better representation of the actual (transversely isotropic) material response.

Figure 7 shows the predicted x-direction tensile response of the 15 fiber RUC as a function of the value of the shear damage parameter, H_{ss}, while the corresponding maximum principal strain fields are plotted (at an applied global strain level of approximately 1%) in Figure 8. It is clear from both figures that, by increasing H_{ss}, which causes an increase in the shear damage induced by local shear stresses, the progression of damage is accelerated in the composite. This highlights the importance of capturing normal-shear coupling in the micromechanics solution in the presence of damage and the value of shear test data for the neat resin.

Figure 9 and Figure 10 show the response and local maximum principal strain plots for applied global longitudinal shear strains, γ_{xz} and γ_{yz}. All cases show good agreement in the initial linear regime, with the 5 fiber RUC loading in yz shear exhibiting slightly higher stiffness.

In general, the effect of the orientation of the applied shear strain (xz vs. yz) has much less of an effect on the longitudinal shear response compared to the effect of the orientation of the tensile loading (x vs. y) on the tensile response. The effect is, however, still present, and, once again, it is minimal in the case of the 15 fiber RUC, suggesting the need to model a good number of fibers within an RUC (to approach a converged representative volume element (RVE)). For the HDP RUC, while localization initiates at roughly the same time for both xz and yz shear, the damage progresses much more quickly under yz shear loading. It is clear from the damage localization patterns in Figure 10 that this is due to the more tortuous path of the damage in the case of xz loading, which leads to the tougher response in Figure 9. In the 5 fiber RUC, the opposite trend is present, with the damage progressing more rapidly, with a straighter path, under xz shear loading. The effect of the RUC geometry itself on the longitudinal shear response is also still present, with nearby fibers leading to earlier damage initiation for the 5 fiber and 15 fiber RUCs. However, the RUC effect is muted compared to the transverse tensile response.

Figure 11 and Figure 12 show the effect of the matrix shear damage parameter, H_{ss}, on the predicted xz shear response of the 15 fiber RUC. For $H_{ss} = 0$, no shear damage can occur, and the effective response remains linear to very high strains when damage due to local normal strains can arise.

As one would expect, increasing H_{ss}, which increases the rate of local matrix shear stiffness reduction in response to local shear stress, has a primary effect on the predicted composite longitudinal shear response. The effect is much greater than the effect of H_{ss} on the predicted transverse tensile response (see Figure 7). Figure 13 and Figure 14 show the predicted transverse (xy) shear response of the composite, along with plots of the local maximum principal strain fields. The 5 fiber RUC predicts slightly higher elastic transverse shear stiffness compared to the HDP and 15 fiber RUCs, which are in close agreement in the linear region. The magnitude of the effect of the RUC geometry on the predicted transverse shear stress-strain response of the composite is similar to its effect on the predicted longitudinal shear stress-strain response. As before, local stress concentrations arising in the matrix between nearby fibers tend to cause early onset of localization due to damage. Finally, all three RVE geometries give rise to straight damage localization paths, leading to similar post-peak xy stress-strain responses.

7. Conclusion

A three-dimensional, anisotropic, progressive damage model, relying on six scalar damage variables, has been developed following the approach outlined by Barbero [1] in the case of plane stress problems. By extending the model to three-dimensional stress states, it is now capable of modeling the behavior of the constituents within a composite, wherein the stress state is inherently three-dimensional. Further, because it is anisotropic, the model could also be applied to any effective anisotropic material; for example the tows within woven composites (though not done herein), which also experience three-dimensional stress states. The damage model is also arbitrary in terms of the interaction among the six damage variables and the stress components, which is controlled by the chosen form of the damage potential. The damage model has been implemented within Abaqus [4] as a user-defined constitutive model. The model was characterized for a neat resin material and then applied to model the transverse tensile, longitudinal shear, and transverse shear response of a unidirectional composite composed of that matrix and carbon fibers. Finite element models representing RUC geometries with HDP, 5 randomly placed fibers, and 15 randomly placed fibers were considered. Periodicity conditions were imposed on the boundaries of the finite element RUC model to ensure representation of the composite material. Results showed that the damage model is capable of

predicting damage localization within a periodic composite in response to both normal and shear loadings for all three RUCs. Further, while the linear portion of the predicted stress-strain curves of all three repeating cells were nearly coincident, significant differences were present once damage initiated due to variations in the represented microstructures. The HDP and 5 fiber RUCs also exhibited significant differences based on the directionality of the applied transverse tension and longitudinal shear loading. In contrast, the 15 fiber RUC showed only minor influence of the loading direction. The influence of the shear damage parameter on the predictions of the 15 fiber RUC was also investigated and shown to significantly soften the post damage initiation response for both applied transverse normal and longitudinal shear loading.

References

[1] Barbero, E.J.. Finite element analysis of composite materials using abaqus. Boca Raton, FL 33487-2742: CRC Press Taylor & Francis Group; 2013.

[2] Kachanov, L.M.. Introduction to continuum damage mechanics. Distributor Center P.O. Box 322, 3300 AH Dordrecht, NL: Kluwer Academic Publishers; 1986.

[3] Kachanov, LM. On the time to failure under creep conditions, Izv. AN SSSR, Ot. Tekhn. Nauk 1985;8:26–31.

[4] Karlsson and Sorensen. Abaqus: Theory Manual. Providence, R.I: Hibbitt, Karlsson & Sorensen; 1992.

[5] Lemaitre, Jean and Chaboche, Jean-Louis. Mechanics of solid materials. The Edinburgh building, Cambridge CB2 8RU, UK: Cambridge university press; 1990.

[6] Chaboche, JL and Kruch, S and Maire, JF and Pottier, T. Towards a micromechanics based inelastic and damage modeling of composites. International Journal of Plasticity 2001;17:411–439.

[7] Krajcinovic, Dusan. Damage mechanics. : Elsevier; 1996.

[8] Voyiadjis, George Z. and Kattan, Peter I.. Damage Mechanics. Boca Raton, FL 33487-2742: CRC Press Taylor & Francis Group; 2005.

[9] Talreja, R. and DCAMM. and DTH.. A Continuum Mechanics Characterization of Damage in Composite Materials. Lyngby. Technical university of Denmark, Danish center for applied mathematics and mechanics. Report: Technical University of Denmark, DCAMM; 1983.

[10] Talreja, Ramesh. Transverse cracking and stiffness reduction in composite laminates. Journal of composite materials 1985;19:355–375.

[11] Pineda, Evan J and Waas, Anthony M and Bednarcyk, Brett A and Collier, Craig S and Yarrington, Phillip W. Progressive damage and failure modeling in notched laminated fiber reinforced composites. International journal of fracture 2009;158:125–143.

[12] Pineda, Evan J and Waas, Anthony M. Numerical implementation of a multiple-ISV thermodynamically-based work potential theory for modeling progressive damage and failure in fiber-reinforced laminates. International journal of fracture 2013;182:93–122.

[13] Bednarcyk, Brett A and Aboudi, Jacob and Arnold, Steven M. Micromechanics modeling of composites subjected to multiaxial progressive damage in the constituents. AIAA journal 2010;48:1367–1378.

[14] Ladevéze, P., Lubineau, G., Violeau, D.. A computational damage micromodel of laminated composites. International Journal of Fracture 2006;137:139 – 150.

[15] Ladevèze, P and Lubineau, G. On a damage mesomodel for laminates: micro–meso relationships, possibilities and limits. Composites Science and Technology 2001;61:2149–2158.

[16] Melro, AR and Camanho, PP and Pires, FM Andrade and Pinho, ST. Micromechanical analysis of polymer composites reinforced by unidirectional fibres: Part II–Micromechanical analyses. International Journal of Solids and Structures 2013;50:1906–1915.

[17] Melro, AR and Camanho, PP and Pires, FM Andrade and Pinho, ST. Micromechanical analysis of polymer composites reinforced by unidirectional fibres: Part I–Constitutive modelling. International Journal of Solids and Structures 2013;50:1897–1905.

[18] Kruch, Serge and Chaboche, Jean-Louis. Multi-scale analysis in elasto-viscoplasticity coupled with damage. International Journal of Plasticity 2011;27:2026–2039.

[19] Chen, Yuli and Ghosh, Somnath. Micromechanical analysis of strain rate-dependent deformation and failure in composite microstructures under dynamic loading conditions. International Journal of Plasticity 2012;32:218–247.

[20] Hansen, NR and Schreyer, HL. A thermodynamically consistent framework for theories of elastoplasticity coupled with damage. International Journal of Solids and Structures 1994;31:359–389.

[21] Bazant, Zdenek P and Cedolin, Luigi. Blunt crack band propagation in finite element analysis. Journal of the Engineering Mechanics Division 1979;105:297–315.

[22] Pietruszczak, ST and Mroz, Z. Finite element analysis of deformation of strain-softening materials. International Journal for Numerical Methods in Engineering 1981;17:327–334.

[23] Bažant, Zdeněk P and Oh, Byung H. Crack band theory for fracture of concrete. Matériaux et construction 1983;16:155–177.

[24] Pineda, Evan J and Bednarcyk, Brett A and Waas, Anthony M and Arnold, Steven M. Progressive failure of a unidirectional fiber-reinforced composite using the method of cells: discretization objective computational results. International Journal of Solids and Structures 2013;50:1203–1216.

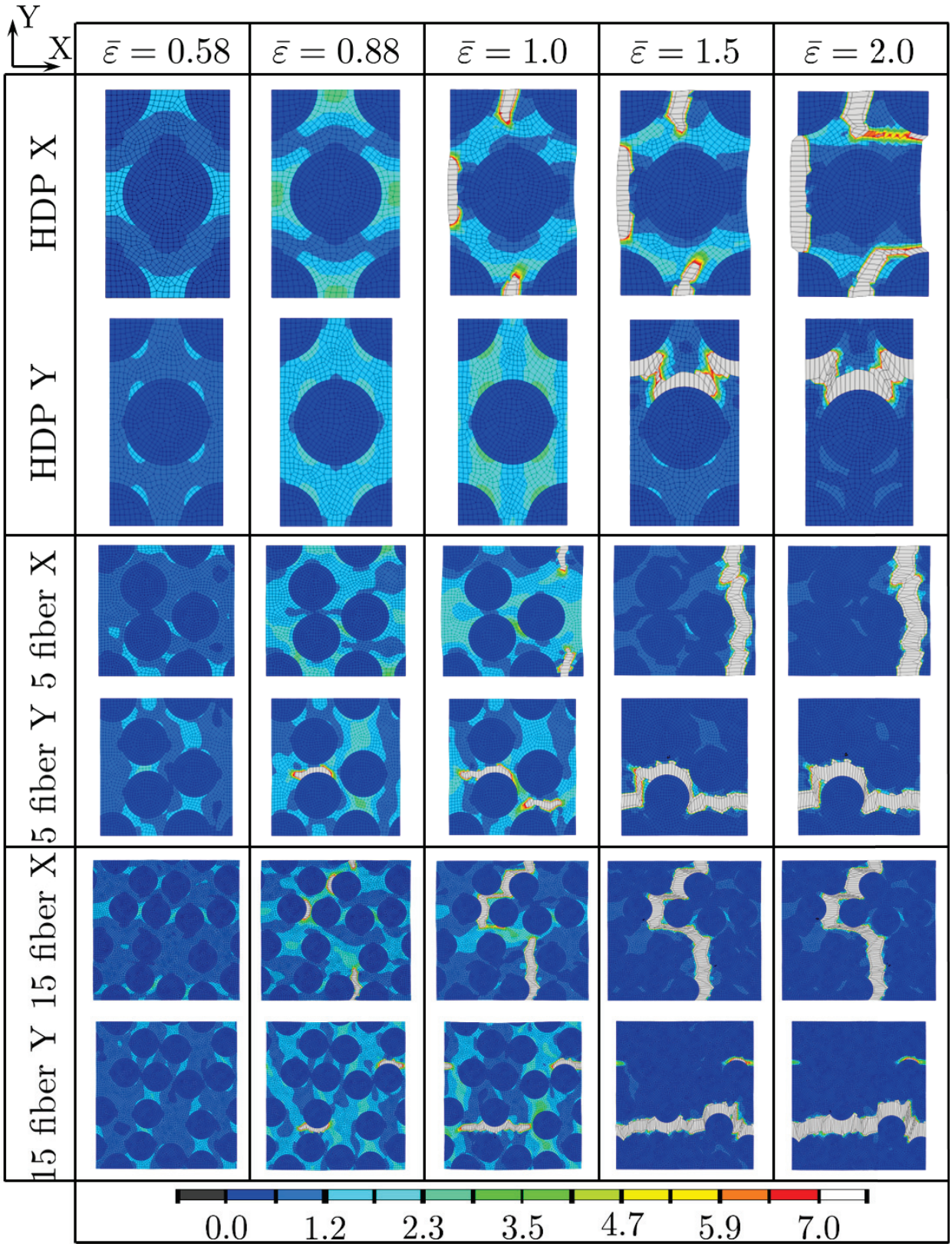

Figure 6: Predicted local maximum principal strain plots during simulated transverse tensile tests at different applied global strains $\bar{\varepsilon}$ as a function of RUC geometry and direction of loading for the case of $H_{ss} = 5$. The deformation scale factor is 5

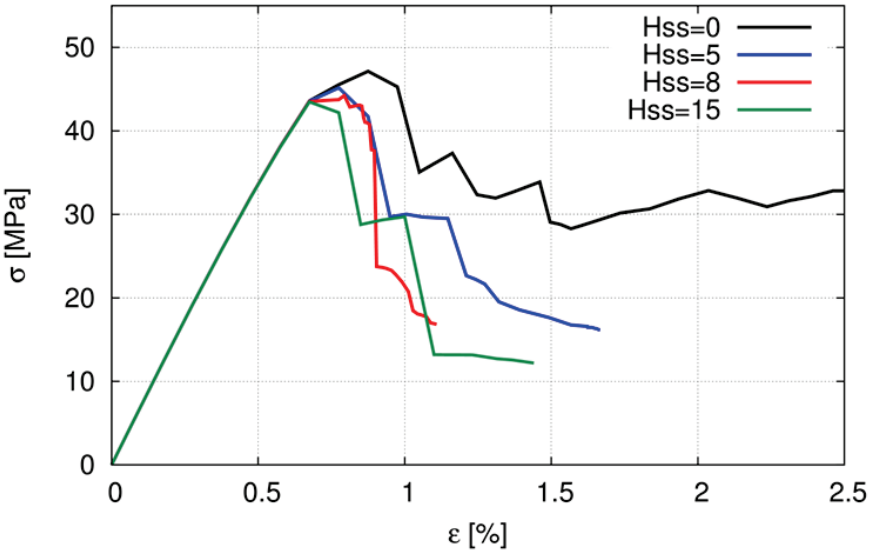

Figure 7: Comparison of the predicted effective composite X-direction transverse tensile response for the 15 fiber RUC as a function of the shear damage parameter, H_{ss}

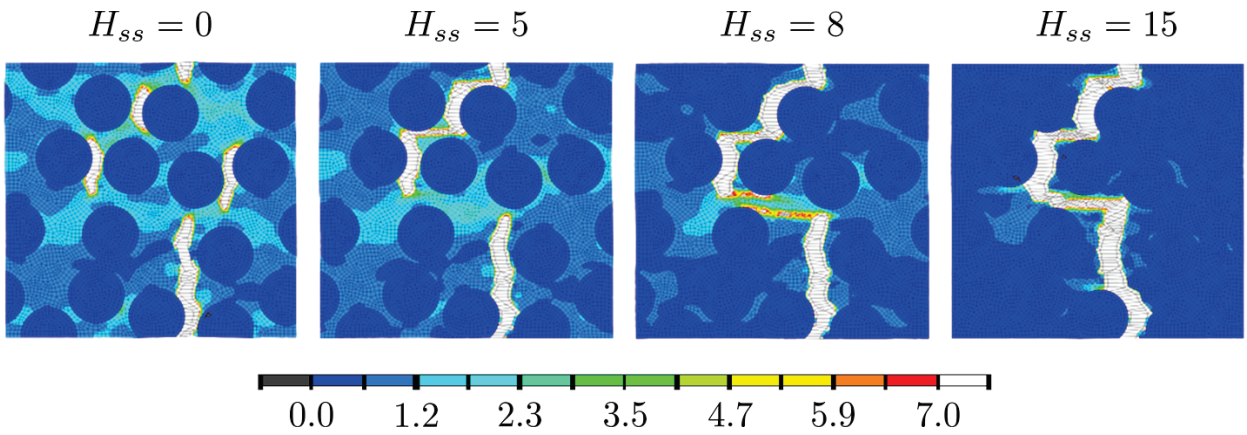

Figure 8: Predicted local maximum principal strain plots during simulated x-direction transverse tensile tests on the 15 fiber RUC as a function of the shear damage parameter, H_{ss}, at an approximate applied global strain of $\bar{\varepsilon} = 1\%$. The deformation scale factor is 5

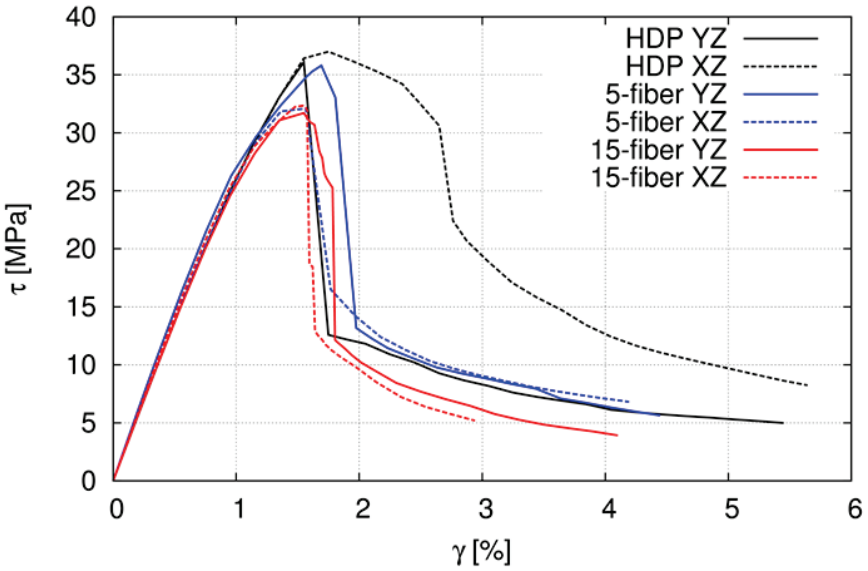

Figure 9: Comparison of the predicted effective composite longitudinal shear response as a function of RUC geometry and direction of loading for the case of $H_{ss} = 5$

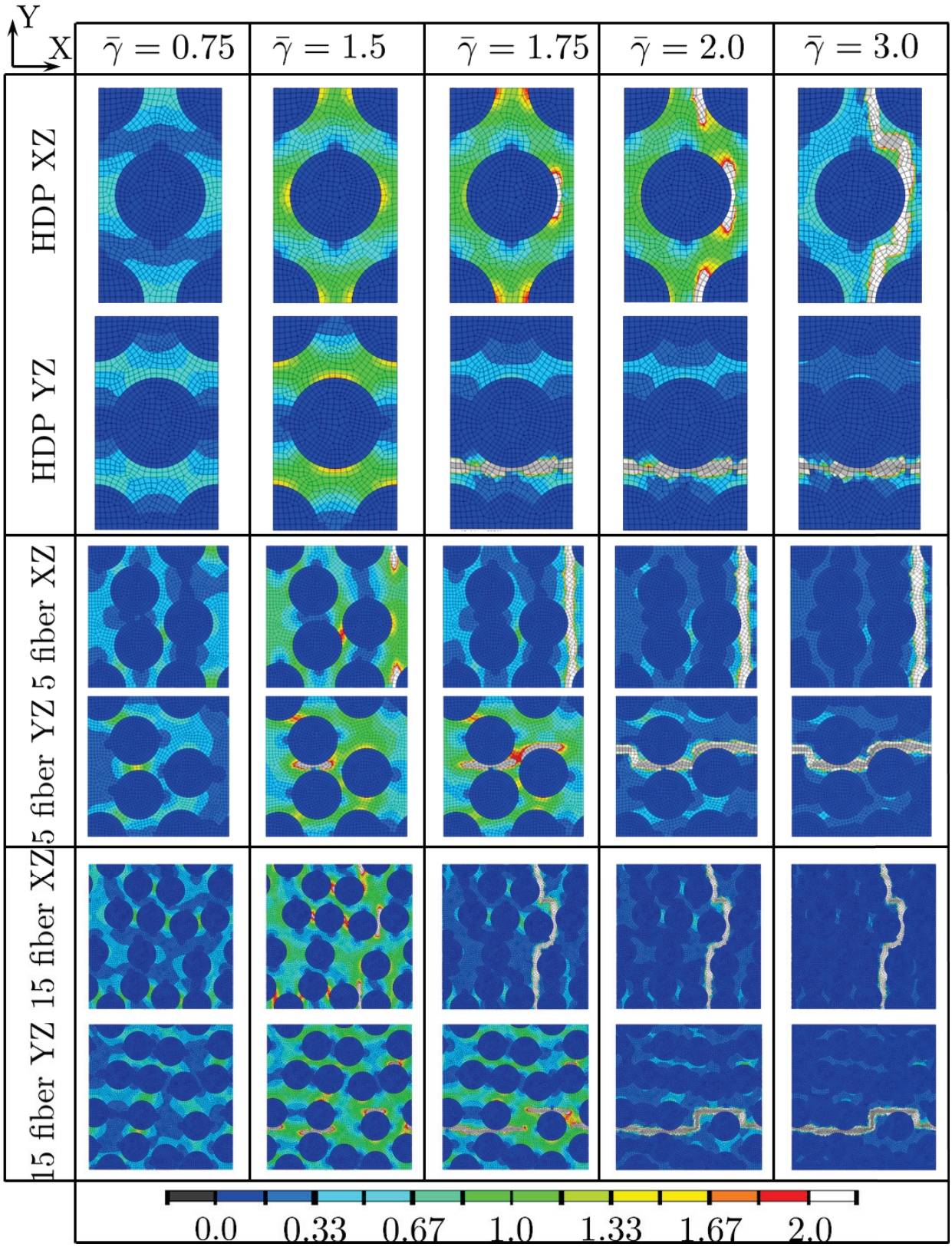

Figure 10: Predicted local maximum principal strain plots during simulated longitudinal shear tests at different applied global shear strains $\bar{\gamma}$ as a function of RUC geometry and direction of loading for the case of $H_{ss} = 5$. The deformation scale factor is 5

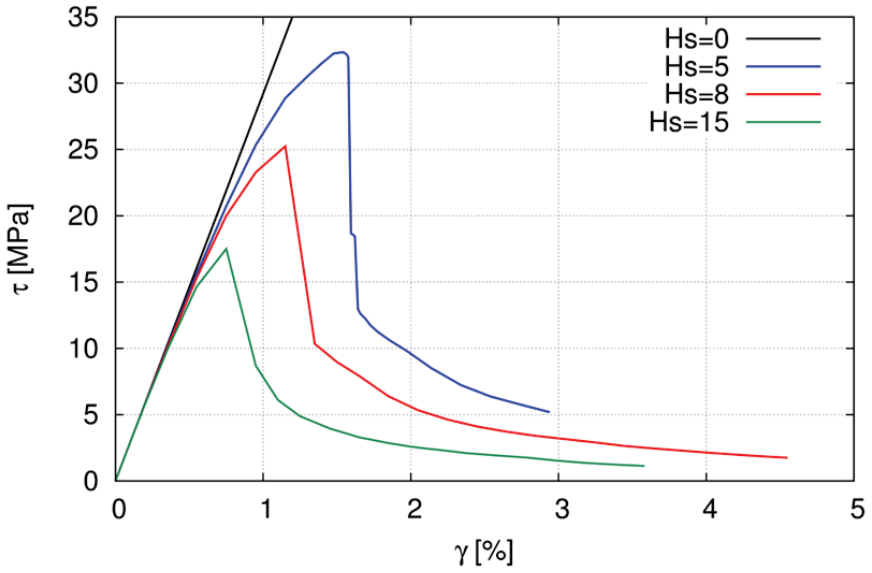

Figure 11: Comparison of the predicted effective composite xz longitudinal response for the 15 fiber RUC as a function of the shear damage parameter, H_{ss}

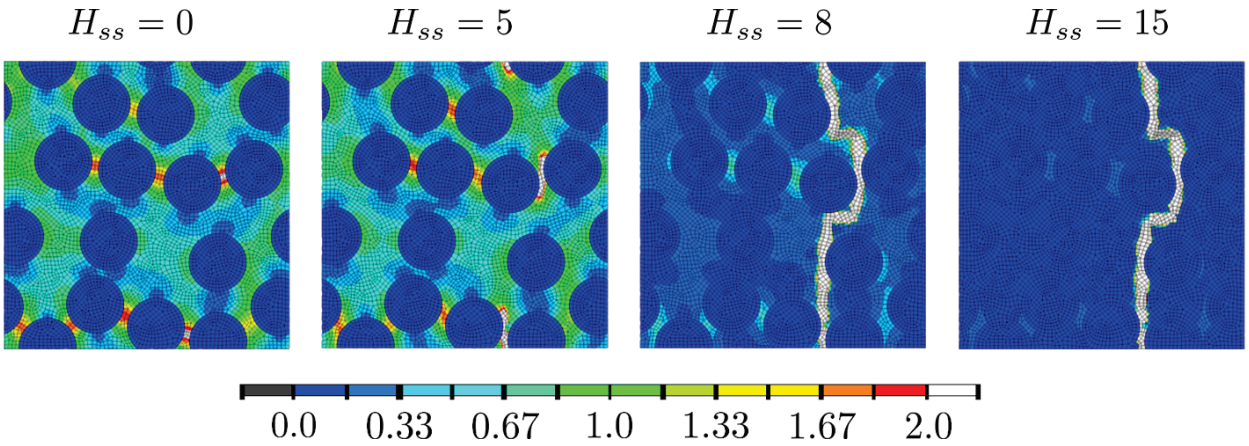

Figure 12: Predicted local maximum principal strain plots during simulated xz longitudinal shear tests on the 15 fiber RUC as a function of the shear damage parameter, H_{ss}, at an approximate applied global shear strain of $gam\bar{m}a$ = 1.35%. The deformation scale factor is 5

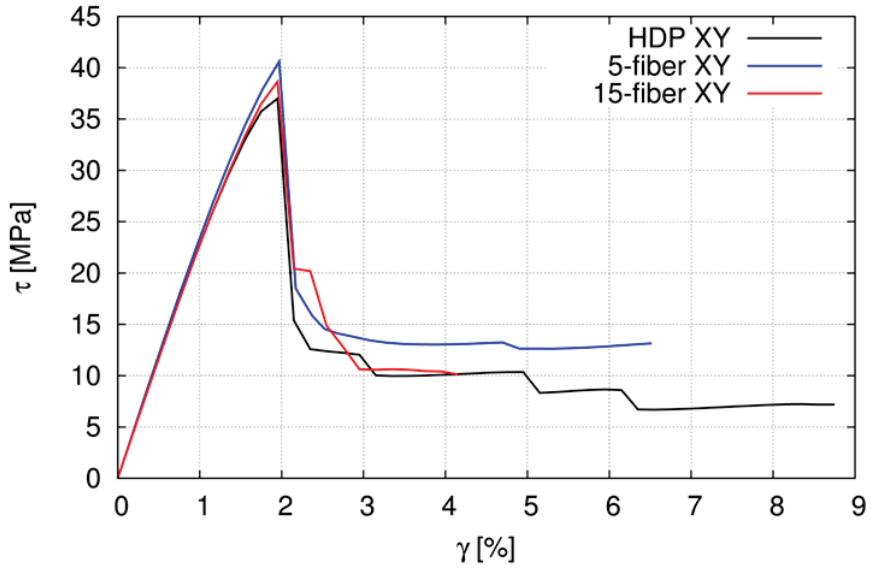

Figure 13: Comparison of the predicted effective composite transverse (xy) shear response as a function of RUC geometry for the case of $H_{ss} = 5$

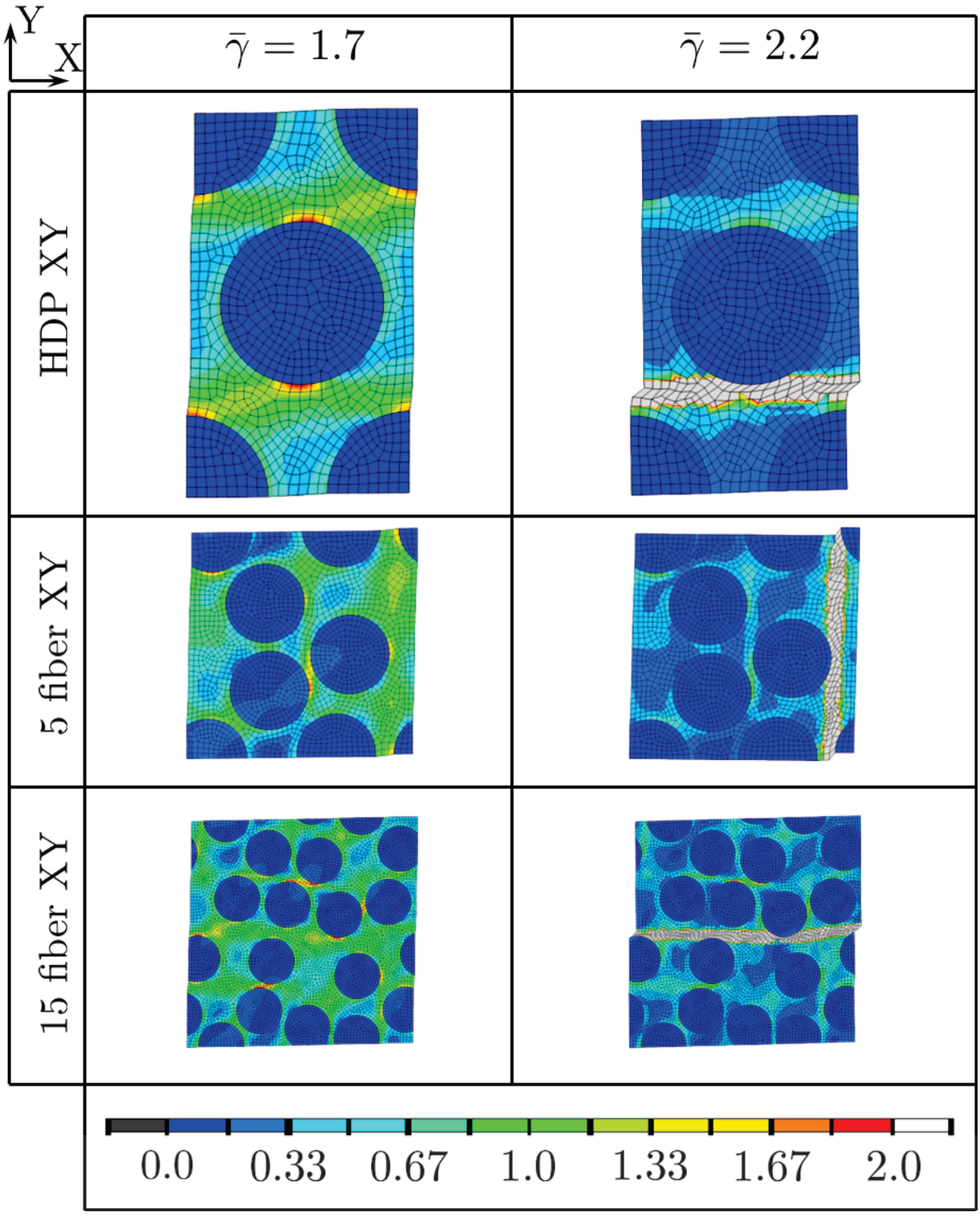

Figure 14: Predicted local maximum principal strain plots during simulated transverse (xy) shear tests at different applied global shear strains $\bar{\gamma}$ as a function of RUC geometry and direction of loading for the case of H_{ss} = 5. The deformation scale factor is 5